Validation of photon collimation techniques for monolithic PET detector calibration

Andrea Gonzalez-Montoro, *Member, IEEE*, Larry A. Pierce II, William C.J. Hunter, *Member, IEEE*, Antonio J. González, *Member, IEEE, and* Robert S. Miyaoka, *Senior Member, IEEE*

***Abstract* — Monolithic based Positron Emission Tomography (PET) detectors have become an attractive alternative to traditional pixelated scintillator modules. One of the main limiting factors to further expand the use of the monolithic approach in commercial PET scanners is the requirement of more complex calibration set-ups than for their pixelated counterparts. These calibration procedures are usually based on Hardware-Collimation methods in which a physically collimated beam source is moved across the front face of the scintillator. These procedures require the use of manifold hardware-setups and are time consuming, especially when dealing with systems composed of many detector modules.**

To reduce complexity and acquisition times of calibration data sets when using monolithic based detectors, we have validated in this work the recently proposed method of using Software-Collimated calibration data for monolithic PET detectors. Software-Collimated methods require less hardware, are easier to implement, and have the potential to be used in an assembled PET scanner. We are evaluating a defined Bias estimator and the overall detector Spatial Resolution using data obtained with the two different collimation techniques. Results showed Bias behavior and Spatial Resolution discrepancies as small as 4.9% between the two data sets for the whole monolithic surface of $50\times 50\times 8$ mm^3. These results demonstrate that Software-Collimated data in combination with accurate positioning algorithms promises to be competitive against traditional Hardware-Collimation procedures. Finally, we have explored and confirmed the use of Software-Collimated data for the calibration step using two procedures, the PC3 method (calibrated data is shown) and Voronoi diagrams.

***Index Terms* — Positron Emission Tomography (PET), Monolithic Blocks, Gamma ray detectors, Calibration**

I. Introduction

Monolithic crystals are becoming widely investigated and used in the development of gamma-ray instrumentation. They are made out of a single piece of scintillator material reducing detector dead areas, thus, improving gamma-rays detectability and efficiency. Monolithic designs allow one to characterize the scintillation Light Distribution (LD) profiles, and thus, to accurately estimate the 3D photon impact coordinates within the detector without the need of using extra hardware or complex positioning algorithms, see for instance [1][2] and references therein. Some advantages, in combination with their lower production costs when compared to small pixel sizes, have made monolithic PET detector designs an attractive alternative to traditional pixelated scintillator crystal designs especially for systems requiring high spatial resolution. However, one of the main limiting factors to the use of monolithic PET detectors in commercial scanners is the complex and time-consuming calibration procedures. Such calibrations are required to correct for nonuniformities, mainly produced by the truncation of the scintillation light distribution at the edges and while rare but possible light yield differences across the scintillation volume.

The calibration procedure when using monolithic PET detector modules has traditionally been performed using a thin beam of 511 keV photons, usually generated by using a small crystal in coincidence with a positron source, see Fig.1 Top. Careful alignment of the point source with the coincidence crystal is required to obtain a useful collimated calibration beam and, moreover, the crystal and source must be moved together as the beam is scanned across the face of the monolithic scintillator during the calibration phase. This procedure requires long acquisition times. In addition, scanning the whole detector surface, using this approach, when the module is already assembled in a PET scanner is impracticable and thus, module re-calibrations require alternative approaches.

Several methods have already been proposed to speed-up and simplify the acquisition of calibration data in monolithic-based systems [3][5]. To avoid the acquisition of calibration data sets, methods based on using uniformity flood maps of the detectors [3], simulations [6], and theoretical models [7][8] for the LD pattern over the crystal have been developed. Other procedures proposed include using acquired training data to obtain the calibration data to train Neural Networks (NNs) [9]. However, these methods require, in general, complex algorithms and are computationally costly.

The present manuscript focuses on combining Software-Collimation methods [10] with two different existent

Submitted 21st October, 2020. This work was supported by grants NIH R01 CA136569, NIH R01 EB002117-04, and NIH 1R41CA180191-01.

A. Gonzalez-Montoro is with the Instituto de Instrumentacion Imagen Molecular (I3M), CSIC – Universitat Politecnica de Valencia, 46022 Valencia, SPAIN and, the Imaging Research Laboratory in the Department of Radiology at the University of Washington, Seattle, WA. USA. (e-mail: andreagm@ stanford.edu).

L. Pierce, W.C. J. Hunter and R.S. Miyaoka, are with the Imaging Research Laboratory in the Department of Radiology at the University of Washington, Seattle, WA. USA.

A.J. Gonzalez is with the Instituto de Instrumentacion Imagen Molecular (I3M), CSIC – Universitat Politecnica de Valencia, 46022 Valencia, SPAIN.

calibration procedures namely: i) PC3 multiplexing [11][12] and; ii) Voronoi diagrams in combination with interpolation methods [5]. These approaches aim to reduce calibration times from days to hours.

Our Software-Collimation method consists of moving a non-collimated point source placed against the entrance face of the scintillator, see Fig. 1 Bottom, to obtain calibration data sets when using monolithic based PET detectors. This methodology makes use of two opposed identical monolithic crystals as would be seen within an assembled PET scanner. After acquisition, coincidence events are analyzed and they are electronically collimated using software tools [13]. The main advantage of our Software-Collimation method is that, since the point source is the only moving part in the set-up, the source/coincidence crystal alignment hardware is not needed. Thus, a monolithic PET detector module could conceivably be calibrated (or re-calibrated) while mounted within a fully-assembled PET scanner, leading to less down-time required for scanner re-calibration.

Despite its many advantages, Software-Collimation methods have not yet been widely adopted. In this work, we perform both Software and Hardware collimation on a monolithic $50 \times 50 \times 8$ mm^3 PET detector module and compare the results. Results shown demonstrated that the recently proposed method of Software-Collimated data acquisition for monolithic PET detectors promises to be competitive against the acquisition of traditional Hardware-Collimation data. In addition, the usability of the data with existent calibration methods (PC3 and Voronoi diagrams) has been also confirmed. Finally, PC3 calibrated data is shown.

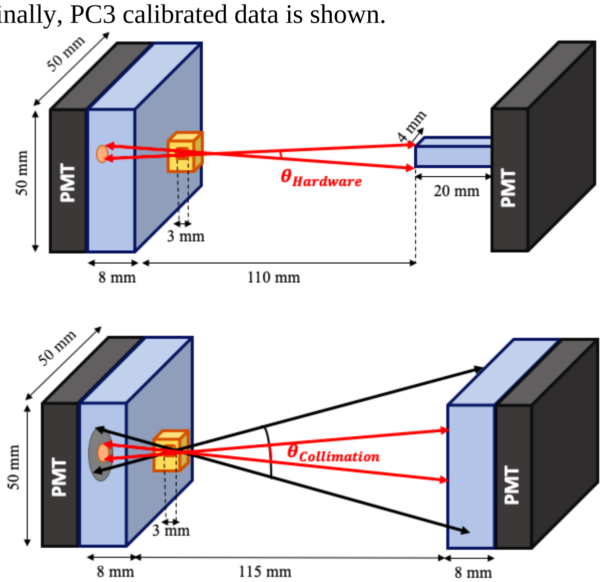

Fig. 1. Illustration of the Hardware- and Software-Collimation setups, top and bottom respectively. A [22]Na point source was used to acquire data. While $\theta_{Hardware}$ is defined by the distance between the detectors and the pixel size used for beam collimation purposes, $\theta_{Software}$ is defined offline.

II. Materials

A. Scintillators and optical elements

Two different volumes of LYSO scintillator material were used for the experiments. The Software-Collimation set-up uses two identical $50 \times 50 \times 8$ mm^3 LYSO monolithic blocks, working in coincidence as later described in detail. The lateral walls (50×8 mm^2) of the scintillators were painted using flat black latex paint and the entrance face (50×50 mm^2) was covered with 0.015-inch Teflon (PTFE) sheet and then a 3M Enhanced Specular Reflector (ESR) layer was added on top of the Teflon.

The Hardware-Collimation set-up made use of one of the previously described monolithic blocks working in coincidence with a $4 \times 4 \times 20$ mm^3 LYSO crystal covered with just ESR material, except the face in contact with the photosensor.

B. Photosensor and Readout

For both the Software- and Hardware-Collimation set-ups, the scintillation blocks (monolithic and pixel) were affixed to an 8×8 channel MAPMT (model H12700, Hamamatsu Photonics, Japan) by means of optical grease (BC630, Saint Gobain, refractive index of 1.47). The monolithic block covered the entire surface of the MAPMT (50×50 mm^2) while the pixelated crystal (4×4 mm^2) was placed at the center of the module used to acquire coincidence data, the uncovered area of the MAPMT was protected using a thick black paper as a light blocker.

The readout electronics developed for the cMICE detector modules [14] was adopted for these experiments. Each module provides 65 output signals, namely: 64 output signals coming from each individual photodetector element of the MAPMT (used for the estimation of the gamma-ray interaction coordinates) + 1 summed-channel output signal. This readout scheme allows one to characterize the scintillation LD produced when a gamma-ray interacts in the monolithic crystal.

During data acquisition, the detector modules were placed inside a dark box. With the use of a thermocouple near the scintillation crystal and a Peltier cooler, the controller (Omega DNi16D) kept the detector temperature almost constant at about $(20.0 \pm 0.1)°C$ for the whole duration of the experiments. The movement of the stepper motors was frequently monitored to ensure an accurate source-crystal alignment.

III. Methods

Both the Software- and the Hardware-Collimation data-sets were generated using a ^{22}Na point source that was 0.25 mm in diameter. The point source was embedded in a $6 \times 6 \times 6$ mm^3 PMMA casing and was positioned, for both set-ups, against the entrance surface of the monolithic detector, i.e. considering crystal surface treatment to be ~ 0.5 mm, the point source was ~ 3.5 mm away from the monolithic crystal entrance face. In both cases, the source was scanned across the surface of the monolithic crystal in small steps of 1.5 mm and data was acquired for 15 minutes at each position. A total of 33×33 beam positions (1089 data points) were collected across the crystal surface for each experimental set-up.

A. Hardware-Collimation data acquisition

Hardware-Collimated data was collected by placing the entrance face of the coincidence pixelated detector at a distance of 110 mm, see Fig. 1 Top. This configuration resulted in a coincidence angle ($\theta_{Hardware}$) that can be estimated by applying:

$$\theta_{Hardware} = atan\left(\frac{D_{size}}{2 \cdot (d_{DD} - d_{DS})}\right) \quad (1)$$

where D_{size}, d_{DD} and d_{DS} represents the scintillator pixel size, the monolithic entrance face – pixel entrance face distance, and the source – monolithic entrance face distance, respectively. In our experimental set-up these values were 4 mm, 110 mm and 3.5 mm, respectively. This works out to approximately 2.1º total aperture for coincidence acceptance.

Figure 2 top is a photograph of the hardware collimation set-up used during the experiment. Two stepper-motors in combination with a custom alignment device were used to ensure the simultaneous movement of the source and the pixelated detector element.

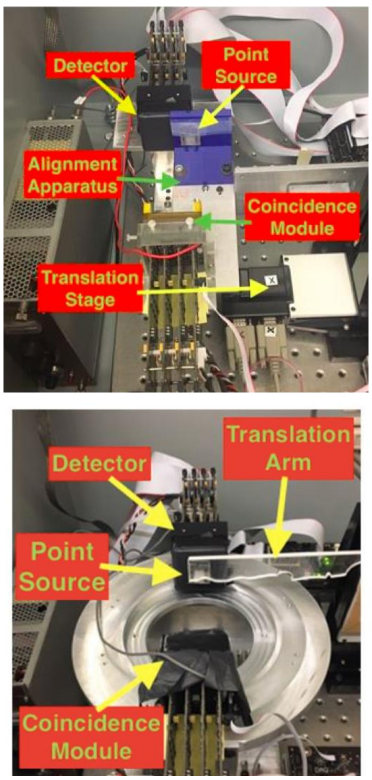

Fig. 2. Photographs of the Hardware- and Software-Collimation setups, top and bottom, respectively. Notice the complexity of the hardware setup in comparison to the software collimation one.

B. Software-Collimation data acquisition

In the Software-Collimated method, the same point source was used but directly attached to a motorized translation arm. The distance between the entrance face of the two monolithic detectors was 115 mm. Figure 2 bottom shows a photograph of this setup. Note that the only moving part in this setup is the point source, which simplifies the acquisition procedure and minimizes the chance of misalignments.

Applying equation (1) but now considering $D_{size} = 50\ mm$ and $d_{DD} = 115\ mm$, a maximum coincidence angle of 24.1º is obtained. We also observed that acquisition times were much faster than in the Hardware-Collimation set-up since the acceptance angle is larger but, not all the events were 511 keV coincidences since more scatter and false-coincidence events (i.e. random events) were also accepted.

C. Data Processing

For each of the two acquisition configurations, an energy window of +/-30 % around the photopeak was applied (358 – 664 keV). Approximately the same number of counts were collected for both the Hardware- and Software-collimation acquisitions. Energy values for each event were estimated as the sum of the 64 output signals. The energy resolution of the block is in the range of 16%.

An Anger positioning method was applied to the 64 output signals for the estimation of the x- and y-photon impact coordinates within the monolithic block. Each impact coordinate was corrected using a cubic polynomial fitted to the known point source positions. Profiles were drawn through these and the Full Width at Half Maximum (FWHM) was computed for each beam position in both the x- and y-directions.

For the Software-Collimated dataset and after calibration was completed, a tolerance *d* (in arbitrary units) was considered as an acceptance angle and defined for the x- and y-values of the Anger position estimate. Coincidence events were filtered according to those events that had x- and y-value absolute differences less than *d* [13][15]. Note that no energy window was applied prior to this filtering of the data.

The threshold value *d* was converted into an acceptance angle after the Anger positions were converted into physical coordinates on the crystal using the 3rd degree polynomial fit. To perform a fair comparison, the values that we chose for *d* were converted to 2.1°, the same as the Hardware-Collimated dataset acceptance angle. Smaller angles could be computed but this may require longer acquisition times, the study of which is outside the scope of this work.

Note that in the Software-Collimation method, all events are considered as normally incident interactions without correcting the x- and y- photon impact coordinates as a function of interaction depth, thus, the estimated LORs angles for the deepest events (closer to the photosensor) are overestimated and rejected since *d* is larger than the defined tolerance. In *Section D.1* we describe a method to correct for this and include data from the deep-penetrating photons thus, increasing the percentage of data kept for calibration.

To quantitively compare these two methods, the metric used was the average detector spatial resolution, measured as the average of the FWHM of the Gaussian distribution profiles obtained for each acquired beam, and a defined Bias estimator. This estimator is based on the absolute difference of the known source mechanical position and the measured value (centroid of the Gaussian fitting applied to each projected LD profile) in the flood map:

$$BIAS = |(x, y)_{real} - (x, y)_{measured}| \quad (2)$$

D. Calibration procedure

We have also validated the viability of the data-sets to be used for the calibration of the monolithic block. We have 3D calibrated (impact planar coordinates and DOI information) the monolithic detector, considering both the Software- and Hardware-calibration data, using the PC3 method. In addition, we have also studied the use of Voronoi diagrams to demonstrate the accuracy of the acquired data within different calibration methodologies. However, no final calibration was performed using Voronoi diagrams because it is outside the scope of this article since calibration was already successful with the PC3 method.

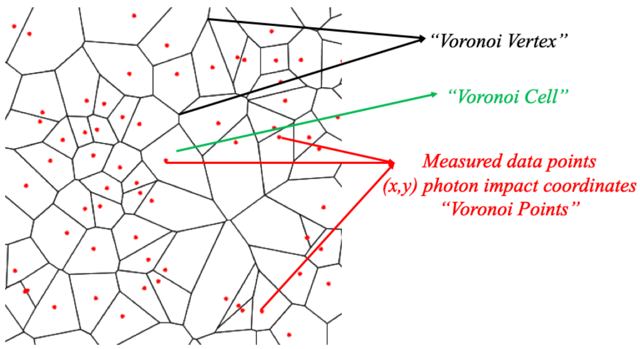

Fig. 3. Example of a Voronoi diagrams including description of the terminology used.

D.1) PC3 method

PC3 calibration algorithm relies on the idea that calibration data lies on a one-dimensional path within the higher-dimensional space of output signals. The method computes the principal components of all calibration data points for initial density threshold-based scatter rejection. See [11][12] for more details on the PC3 algorithm.

For each one of the acquired beam positions, the principal components of the calibration data were computed and the output data events were then transformed into the principal component coordinates via change-of-basis. This provided a density profile of events according to the principal component coordinate values. Upper and lower thresholds were defined as a fraction of the maximum density [11], and all the events that fell outside of this window were rejected as scattered events. The remaining calibration data events were then projected and the principal components of the projected data were computed. Finally, using a 2-stage Gaussian maximum likelihood positioning algorithm, two sets of lookup tables were recorded and used to provide the Euclidean norm of the events for each (x, y) coordinate.

Notice that, since the Software-Collimation method rejects most of the events interacting closer to the photosensor and the PC3 calibration methodology requires photons at all depths, after computing the Anger coordinates and applying the Software-Collimation threshold (*d*), we defined a new acceptance window (*d' > d*) around the detector under calibration. Dimensions (*d'*) are defined by the accepted data in the reference window. Then, we went back over all the data to find all event in the detector under calibration that fell within the new window (*d'*) thus considering the deepest interactions and included them in the calibration.

D.2) Voronoi Diagrams

Voronoi diagrams are mathematical structures that can be defined as a partitioning of the plane into various convex polygons called Voronoi cells. For each cell, an arbitrary point, called the Voronoi Point is defined as the point of the plane closest to the cell surroundings.

Thus, the number of polygons corresponds to the number of points contained in the plane [16]. See Fig. 3 for a better understanding of this terminology. The introduction of these diagrams was already proposed [17][18] and also validated in pixelated-based PET detectors, for energy calibration procedures [19] and crystal identification in multiple-layer configurations [20]. Moreover, its use has been recently validated against standardized calibration methods used in monolithic based PET detectors [5], showing promising results for the calibration of the 3D impact coordinates and also energy.

The implementation of Voronoi diagrams to confirm the possibility of using the Voronoi method in combination with the Software-Collimated calibration data was computed using Python [21], and required previous knowledge of the x- and y-photon impact coordinates. Note that only the usability of the data in combination with Voronoi diagrams was studied. Final calibration of the monolithic detector using Voronoi diagrams was not performed.

Therefore, in the present work we are reporting on the accuracy for determining the impact regions using Hardware-Collimation data and Software-Collimation data plus Voronoi diagrams. In addition, 3D calibrated data and performance evaluation are reported for both the Software- and Hardware-Collimation plus PC3 method.

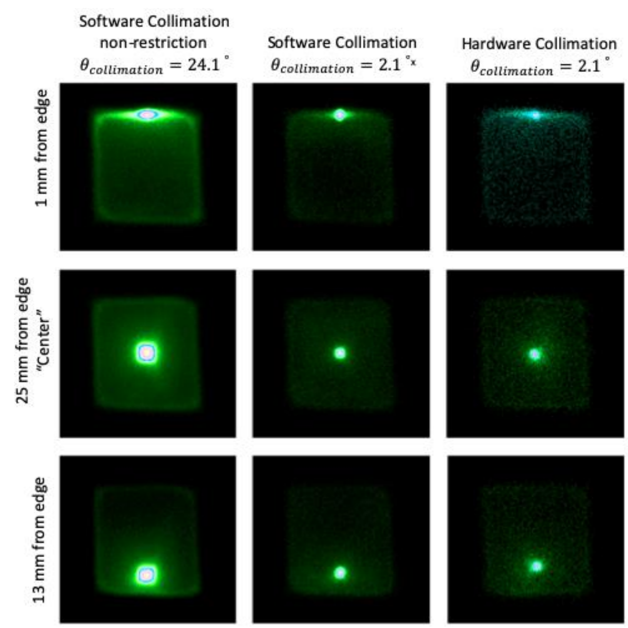

Fig. 4. Flood maps of the ^{22}Na source at three different position: 1mm (top), 25 mm (center) and 13 mm (bottom) from the crystal edge. The flood maps, from right to left, are shown for the Hardware Collimation with $\theta_{Collimation}$ = 2.1°, Software collimation with $\theta_{Collimation}$ = 2.1°, and Software Collimation when non-angular restriction is applied, respectively.

IV. Results

A. Validation of the Software-Collimation methodology

The use of Software-Collimation has been evaluated by analyzing both the x- and y-projections of the LD profiles for each one of the 33 × 33 beam positions. The same procedure was applied for both the Software- and Hardware-Collimation acquired data.

Figure 4 shows examples of flood maps obtained at three different beam positions, namely: 1 mm, 25 mm (center of the block) and 13 mm from the crystal edge, respectively. Left, center and right columns of Fig. 4 show these flood maps for the Software-Collimation set-up when not applying any angular restriction; for the Software-Collimation set-up when applying a collimation angle of $\theta_{Software}$ = 2.1° and; for the Hardware-Collimation set-up in which, as estimated using Eq. 1, $\theta_{Hardware}$ = 2.1°, respectively. As it can be appreciated, when no angular restriction is applied to the Software-Collimation more background noise is accepted and the beam profiles are wider, since the only restriction is imposed by the geometry of the experimental set-up, i.e. position of the source with respect to the detector being calibrated.

To estimate the positioning accuracy of each method the defined Bias estimator was calculated. Figure 5 shows the Bias obtained through the y-axes (direction of movement of the source) for the 33 positions for the central row of the crystal. We have decided to only show plots for the central row to simplify the presentation of the results but similar curves were obtained for all the other rows. Note that near the edges, for the outermost columns/rows, the overall Bias curve worsens to values in the range of 3.5-4.5 mm due to the truncation of the LD profiles. Both the Hardware and Software collimation set-ups perform similar.

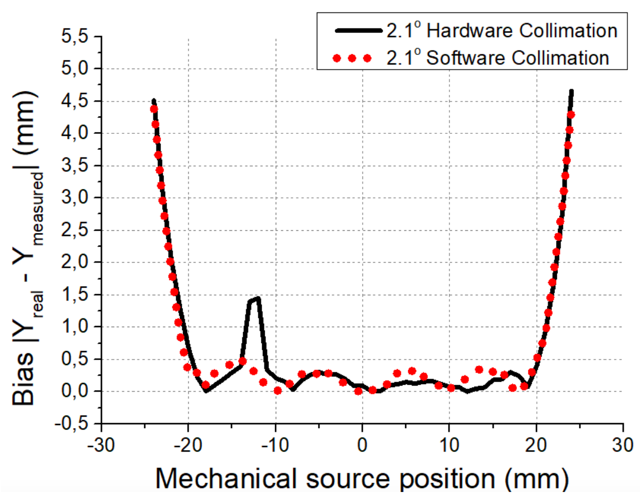

Fig. 5. Bias vs Mechanical source position for the central row of acquisitions.

FWHM calculations of the Hardware and Software collimated calibration beams in both the x- and y-directions for each beam position were performed. Figure 6 depicts the non-calibrated measured FWHM for each beam position across the central row of the crystal for the y- and x- profiles, respectively and for both the Hardware- and Software-Collimation data with $\theta_{Collimation}$ = 2.1°. Error bars are estimated as the error provided by the Gaussian fitting to the mean value. Note that, in the plots shown here the source displacement was across the y- direction. As expected, similar curves are obtained when analyzing all the other rows and columns.

Calibration beam FWHM values for each non-calibrated beam position, defined as $FWHM_{(x,y)}$, was finally estimated as the quadratic average of the FWHM measurement of the x- and y- profiles at each individual beam position as $\overline{FWHM_{(x,y)}} = \sqrt{FWHM_x^2 + FWHM_y^2}$. Figure 7 shows these results as contour plots for all source positions and for both set-ups ($\theta_{Collimation}$ = 2.1°). Average values are better at the center and worsen toward the edges and corner of the of the monolithic detector block. Note that the x- and y- axis of the contour plots represent the monolithic block dimension (50 × 50 mm^2).

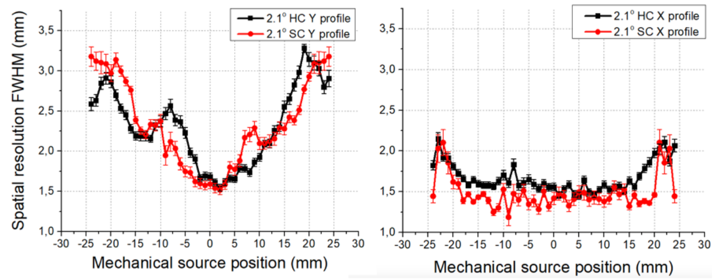

Fig. 6. Spatial Resolution FWHM measured through Gaussian fitting for the y- (left) and x- (right) source profiles, respectively, for each beam position across the central rows of the crystal. Black points stand for the Hardware collimation set-up while red points stand for the Software Collimation set-up. In both cases $\theta_{Collimation}$ = 2.1°.

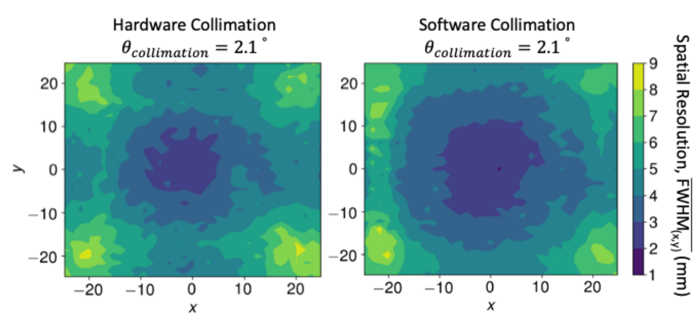

Fig. 7. Contour plots showing the $\overline{FWHM_{(x,y)}}$ average values for each one of the 33×33 measured source positions, for the two collimation set-ups.

Table I. Average collimation beams width values, before detector calibration, measured when considering different areas over the monolithic surface for the Hardware and Software Collimation set-ups, respectively.

Scintillator area (mm)	Hardware Collimation 2.1° (mm)	Software Collimation 2.1° (mm)	Deviation
[-25, 25]	4.8±1.2	4.4±1.3	4.3 %
[-19, 19]	4.3±1.1	3.5±0.8	9.1%
[-13, 13]	3.1±0.5	2.6±0.4	8.7%

To evaluate the dependency of the proposed Software-Collimation method as a function of the beam position, Table. I depicts the average $\overline{FWHM_{(x,y)}}$ beam width values when considering three different areas over the monolithic block surface, namely: i) an area of 50 × 50 mm^2, all the 33 × 33 beam positions were considered; ii) an area of 38 × 38 mm^2 and thus, the 5 outer source positions in each direction are rejected and; iii) an area of 26 × 26 mm^2 when the 10 outer source positions in each direction are rejected. Figure 8 shows the crystal area considered in each case. Error values are estimated as the standard deviation of the average $FWHM_{(x,y)}$. Average values of $\overline{FWHM_{(x,y)}}$ are 4.8±1.2 mm, 4.3±1.1 mm and 3.1±0.5 mm; 4.4±1.3 mm, 3.5±0.8 mm and 2.6±0.4 mm; were achieved for each one of those areas for the Hardware- and Software- collimation set-ups, respectively, when $\theta_{Collimation}$ = 2.1°. A deviation of 4.3% was observed between the two calibration beam profiles when considering the whole 50 × 50 mm^2 detector surface. This statistical deviation increases to 9.1% and 8.7% when considering reduced areas, due to more uniform resolution, as shown in Figure 7, when applying the Software-Collimation methodology.

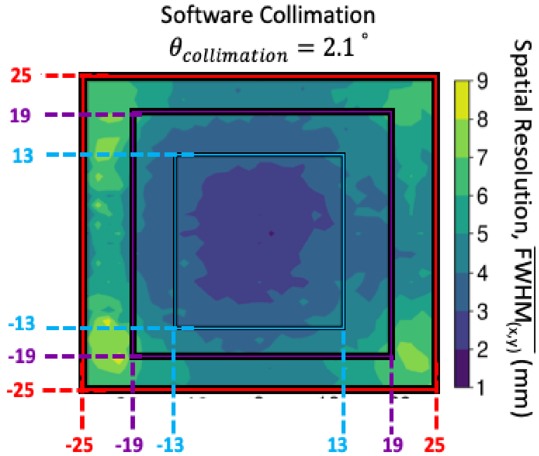

Fig. 8. Monolithic crystal area considered for the evaluation of the detector average spatial resolution. Areas of 50 x 50 mm^2 (red), 38 x 38 mm^2 (purple), and 26 x 26 mm^2 (blue), have been considered.

B. Calibration procedures

Once the Software-Collimation methodology was demonstrated to perform similarly to the traditional Hardware-Collimation for monolithic based PET detectors, we explored its combined use with two different calibration methodologies namely: PC3 method and Voronoi diagrams. The methods proposed here focus on the precise determination of the XY planar coordinates including correction of nonuniformities that result of the different detector components or manufacturing processes between different blocks [23][24].

B.1) PC3 calibration

The PC3 calibration methodology has been applied to both the Hardware- and Software-Collimation data-sets, see Fig. 9 Top and Bottom, respectively. The multiplexing step for PC3 was performed using the same methods as detailed in [11] [12].

In general, results show good performance but slightly heterogeneous half-max contours maps at the edge regions. Slightly worse delineation was obtained for the Hardware-Collimation data set closer to the edges, due to the edge problems associated with monolithic based detector designs. For this reason, the two-outer row/columns were not considered for the average spatial resolution estimation when using the Hardware-Collimation data, thus, an area of only 47 × 47 mm^2 could be considered. For the Software-Collimation data all the 50 × 50 mm^2 area was able to be considered demonstrating the better performance of this methodology for acquiring calibration data.

Figure 10 right shows the contour average $\overline{FWHM_{(x,y)}}$ for the Software-acquired data. Average resolution values $\overline{FWHM_{(x,y)}}$ of 2.3±0.6 mm, 2.0±0.3 mm and 1.9±0.3 mm; 2.3±0.6 mm, 2.0±0.3 mm and 2.0±0.3 mm; were achieved for each one of those areas for the Hardware- and Software-Collimation set-ups, respectively, when $\theta_{Collimation}$ = 2.1°. Error values are estimated as the standard deviation of the quadratic average of the $FWHM_{(x,y)}$. Table II summarizes those values and includes the deviation performance when using Hardware- or Software-Collimated data. Note that in the Hardware collimation data the 2 outer most rows and columns were not included in the calculation.

The PC3 methodology also allows one to calibrate the DOI coordinate. Fig. 10, left, shows the number of events per depth bin for the Software-Collimation data, over many different beam positions (thin colored lines) as well as the theoretical Beer–Lambert distribution (red bold line) demonstrating a good accuracy of the DOI estimation in the 8 mm thick monolithic block.

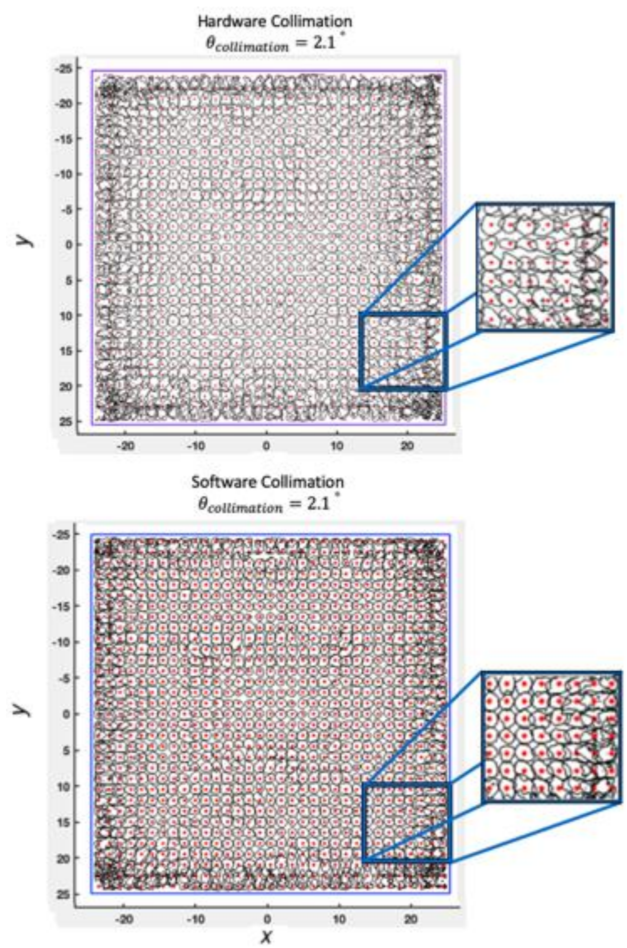

Fig. 9. Half-contour regions obtained for the Hardware- (Top) and Software- (Bottom) collimation set-up using the PC3 calibration method.

B.2) Voronoi Calibration

We have also explored the option to calibrate the detector using Voronoi diagrams since it has been demonstrated that this method may allow resolving events across the entire surface of the detector thus, increasing overall system sensitivity [5].

We have plotted the (x, y) 1089 measured positions for both the Hardware- and Software- collimation set-ups. The Voronoi diagrams have been computed using a specific Python function (Voronoi) [21]. Figure 11 shows the determined Voronoi cells for the Hardware- (top) and Software-Collimation (bottom) data-sets. As it can be appreciated the 33×33 beam positions were successfully identified in both cases and the Voronoi cells were precisely delineated. As in the previous PC3 case worse identification performance was observed at the edge regions but overall results are good. These results demonstrate the viability of Software collimated data to be used in combination with this calibration methodology.

Following [5], the next steps will be to determine the Voronoi factors defined as the ratio between the known source position and the measured one. Finally, interpolation methods will be applied to calibrate the entire monolithic detector. Our goal was to demonstrate the option of combining Software-Collimated data with Voronoi methods. We will explore the calibration performance in a future work in which we also plan to include DOI calibration.

Table II. Average spatial resolution values, before after PC3 calibration, when considering different areas over the monolithic surface for the Hardware and Software Collimation set-ups, respectively. Note that in the Hardware collimation data the two outer most row and columns were not included in the calculation.

Scintillator area (mm)	Hardware Collimation 2.1° (mm)	Software Collimation 2.1° (mm)	Deviation
$[-23.5, 23.5]^{HC}$ $[-25, 25]^{SC}$	$(2.3\pm0.6)^{HC}$	$(2.3\pm0.6)^{SC}$	0 %
[-19, 19]	2.0±0.3	2.0±0.3	0%
[-13, 13]	1.9±0.3	2.0±0.3	5%

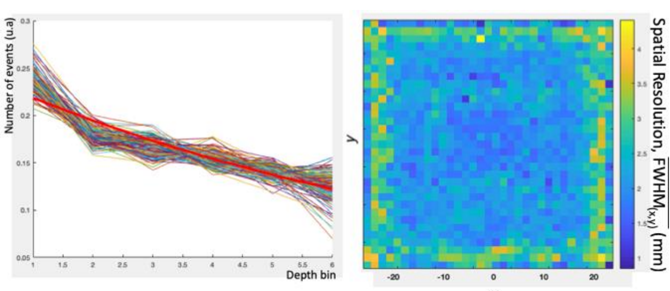

Fig. 10. Left, distribution of the number of events positioned per depth bin for the Software-collimation experiment. Horizontal axis indicates the bin depth number (with 1 being the entrance face of the crystal). The vertical axes indicate the fraction of events in a given depth bin. The distribution for each beam in rows/columns are shown as the thin colored lines. The theoretical Beer–Lambert distribution is shown as the thick red line superimposed on each. Right, contour plot showing the $\overline{FWHM_{(x,y)}}$ average values for each one of the 33 x 33 measured source positions, for the Software-collimation set-up and the PC3 calibration method.

V. DISCUSSION

In the present article, we have focused on validating the accuracy of using Software-Collimated generated data as an alternative to the traditional use of Hardware-Collimated sets for the calibration of monolithic based PET detectors. Our main aim was to simplify the acquisition of calibration data that usually requires long measurement times and complex hardware set-ups.

We have compared the accuracy of both calibration data sets by making use of a defined Bias metric, accounting for the mispositioning of the events, and of the detector average Spatial resolution, $\overline{FWHM_{(x,y)}}$. Finally, we also reported on the accuracy of the Software-Collimated data to be used in combination with current calibration methodologies.

In the case of the Hardware-Collimation set-up the experimental design was more complicated, see for instance Fig. 2. The experiments required a perfect alignment between the source and the scintillator pixel element since they had to be moved simultaneously. The use of this experimental set-up is impractical when the detector modules are already assembled in a PET system. Thus, re-calibrations of the detectors are hardly possible following this approach. On the contrary, the experimental set-up used to acquire Software-Collimated data was more simplistic since the only moving part was the radioactive source. Thus, it can be performed for re-calibration purposes when the modules are already assembled in the final system.

One of the key parameters to be considered in this comparison is the maximum acceptance angle, $\theta_{Collimation}$, that was defined by the experimental set-up geometry. In the case of the Hardware-Collimation, such angle was determined by the distance between the detectors, the source position and the cross-section of the pixel used for generating collimated data, see Eq. 1. In this particular case, the defined angle was $\theta_{Collimation}$ = 2.1°. For the Software-Collimation experiments the maximum angle was defined by the relative position between the source and the two detector modules which in our case lead to a $\theta_{Maximum}$ = 24.1°. One of the main advantages of the Software Collimation data is that a tolerance angle for the data can be later defined during data processing. In this case, we fixed that value to $\theta_{Collimation}$ = 2.1°, to provide a fair comparison with the Hardware-Collimation experiments. The acquisition times, using the same radioactive source, required to obtain an equivalent number of filtered events for this level of angular filtering was ~ 4-5 minutes. Note however that smaller acceptance angles can be selected improving average impact estimation accuracy and Bias [13] but this would require more statistics and, thus, a trade-off between resolution and number of collected calibration events has to be considered.

Flood maps were obtained for each one of the 33×33 beam positions for each experimental set-up. As shown in Fig. 4, the flood maps obtained for the Hardware- and Software-Collimation experiments are very similar. However, the Software-Collimation acquired data seems to be more accurate closer to the edges of the crystal than the Hardware-Collimation data, thus, partially mitigating the impact of the undesired edge effect present in monolithic PET detectors [22]. We hypothesize that, the worse performance of the Hardware-Collimation data may be due to the restrictions imposed by the more complex Hardware set-up, such as, alignment problems between the pixel element and the source, or between the pixel and the opposite detector. The measured Bias showed a good agreement between both methods.

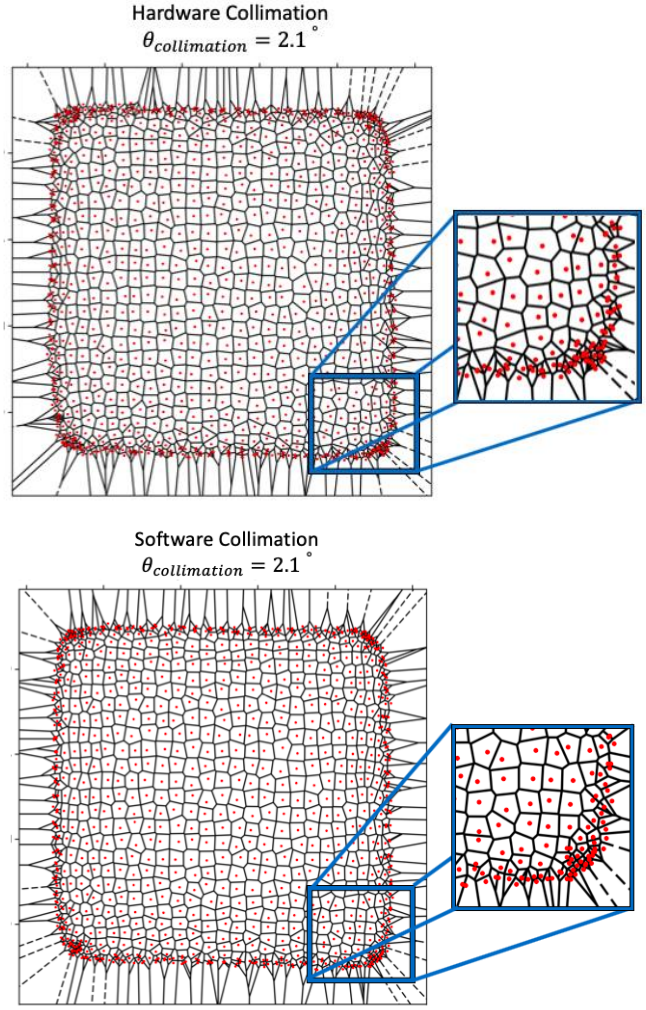

Fig. 11. Voronoi diagrams obtained for the Hardware (Top) and Software (Bottom) Collimation set-ups, respectively, when considering $\theta_{Collimation} = 2.1°$. Zoom of one corner is also shown for both cases to better see how the Voronoi delineation performs at the corners.

The same LD profiles were also used to exhaustively evaluate the detector average spatial resolution before calibration, $\overline{FWHM_{(x,y)}}$, for both the x- and y- profiles. The plot in Fig. 6 shows the FWHM of the Gaussian fitting, for the same 33 positions. As expected, the resolution worsens towards the edge of the crystal in the direction of movement. Looking only at the central region, spatial resolution values are similar for both the x- and y- projections (the entire LD is collected in both directions). Finally, to compare both methods, the $\overline{FWHM_{(x,y)}}$ was computed as the quadratic average of the FWHM values measured for the x- and y- profiles at each position. Figure. 7 shows the contour plots including those values. The Software-Collimation method retrieves more uniform resolution values. We estimated the average spatial resolution for three different areas for the Hardware- and Software- collimation set-ups. The standard deviation was found to be smaller for the Software-Collimation data set (more uniform data). An overall deviation as small as 4.3% was achieved between the Hardware- and Software- collimation spatial resolution values, when considering the full detector area thus, validating the use of Software-Collimation data to provide accurate calibration flood maps when using monolithic based PET detectors. The Software-Collimation data rejects most of the deepest interacting events (~ 17% of the total detected counts), it would be interesting to further investigate on the DOI correction to further increase the number of calibration event accepted.

Once the accuracy of Software-Collimation data was demonstrated, we calibrated the detector using both data sets in combination with the PC3 method. As depicted in Fig. 9 Top and Bottom, better delineation of the events closer to the edge of the monolithic crystal is achieved when considering the Software-Collimated data. Notice that the PC3 method in combination with Hardware-Collimation data was only able to accurately calibrate events in an area of 47×47 mm^2 negatively impacting event recovery and detector sensitivity. However, the full detector area of 50×50 mm^2 was properly resolved when using Software-Collimation data, further demonstrating the feasibility of using the proposed methodology. The average $\overline{FWHM_{(x,y)}}$ spatial resolution values for the calibrated beam positions are shown in Table II. As shown in the right column, after calibration both data sets perform almost identical except closer to the edges, where the Software-Collimated data had a slightly tighter variance overall, especially at the edges.

Contour FWHM maps show a more homogeneous resolution across the detector when compared with the non-calibrated Anger positioned Software-Collimation data. In addition, the DOI coordinate was effectively identified and calibrated as shown in Fig.10. While Depth of Interaction (DOI) is a critical parameter to be evaluated in detail, DOI resolution was not fully evaluated in the present analysis since our main goal was to validate the proposed experimental methodology. However, since the (x,y) coordinates are well preserved, non-significant discrepancies are expected for the DOI when using one of the proposed methods. In the future, we plan to evaluate the DOI accuracy through oblique angled beam experiments. Note that PC3 method is already providing 3D calibrated data, thus, we can state that 3D calibrated data combining the Software-Collimation methodology plus PC3 calibration has been experimentally shown to provide high positioning resolution.

Finally, as a complementary analysis and in order to check the scope of our findings, we have explored the option of using the generated data in combination with Voronoi calibration techniques. We have demonstrated that it is possible to identify the Voronoi cells for all the 33×33 beam positions. As depicted in Fig. 12, the Voronoi approach identifies events in the whole detector surface. Further, almost identical Voronoi diagrams have been obtained for the two data sets, promoting the use of the Software-Collimated data for the detector calibration. Performing the full calibration of the detectors using Voronoi diagrams once the cells are identified has been already demonstrated in the literature [4][5], but it is out of the scope of this paper.

VI. Conclusion

We have described and validated a Software-Collimation methodology to provide accurate calibration data when using monolithic based PET detectors. The method was validated against the traditional approach of using a small crystal element coincidence detector to mechanically collimate the photon flux.

When using a similar angular acceptance angle for coincidence events, the Software-Collimation method performed as well as the traditional Hardware-Collimation method according to beam spot size (i.e., resolution). An average spatial resolution discrepancy as small as 4.3% was achieved when considering events in the whole 50 × 50 mm^2 detector surface. Evaluation of the DOI coordinate through oblique angle beam illumination experiments will be performed in the future.

Finally, we have also demonstrated the viability of the Software-Collimated acquired data to be used in combination with existent calibration methods used in monolithic detectors, such as the PC3 method [12]or Voronoi diagrams [5]. A full 3D calibration of the detector was performed using the PC3 method showing good overall performance in terms of XY spatial resolution, positioning and, also DOI information.

Summarizing, the advantages of Software-Collimation over Hardware-Collimation: 1) set-up is mechanically less complex; 2) it can be carried out in assembled scanners; 3) computational requirements are much lower; 4) supports the use of shorter calibration scan times (~ 1/3 reduction in time compared with conventional Hardware-Collimation methods); 5) potential to use multi-point source calibration arrays without mechanical collimation to further speed up the calibration process. Other works have also explored the use of Software-Collimation versus the traditional Hardware-Collimation approach. For instance, in [13] the authors focused on providing an accurate method to estimate the intrinsic spatial resolution of thick monolithic blocks using Software-Collimated data. That work was based on using SiPMs instead of MAPMT and explored different monolithic thicknesses. The present analysis further supports those findings and we encourage the use of monolithic based PET detectors in commercial scanners since the acquisition of calibration data can be simplified by using Software-Collimation methods.

Acknowledgment

This work was supported by grants NIH R01CA136569, NIH R01 EB002117-04, and NIH 1R41CA180191-01.

The realization of the presented experiments was part of the VISIT program performed at the department of Radiology at the University of Washington by Dr. A. Gonzalez-Montoro under the supervision of Dr. R. S. Miyaoka.

References

[1] C. S. Levin, "Detector design issues for compact nuclear emission cameras dedicated to breast imaging," Nucl. Instrum. Methods. Phys. Res. A, vol. 497, no. 1, pp. 60–74, 2003.
[2] A. J. Gonzalez, et al "A scintillator geometry suitable for very small PET gantries," Journal of Instrumentation, C12018, 2017.
[3] S. España, et al., "Fast calibration of SPECT monolithic scintillation detectors using un-collimated sources," Phys. Med. Biol. 58 (14), 2013, 4807-4825.
[4] M. Freire, et al., "Calibration of PET Detectors Based on Monolithic Blocks Using Voronoi Diagrams," IEEE Nucl. Sci. Symp. Med. Imag. Cond (NSS/MIC) (2018).
[5] M. Freire, et al., "Calibration of Gamma Ray Impacts in Monolithic-Based Detectors Using Voronoi Diagrams," IEEE Trans. Rad. Plasma Med. Sci., Vol. 4, No. 3, 2020.
[6] S. Moehrs, et al., "A detector head design for small-animal PET with silicon photomultipliers (SiPM)," Phys. Med. Biol., Vol. 51, 2006.
[7] M. Morrocchi, et al., "Development of a PET detector module with Depth of Interaction capability," Nucl. Instrum. in Phys. Res. A., Vol. 732, 2013.
[8] T. Ling, et al., "Parametric positioning of a continuous crystal PET detector with depth of interaction decoding," Phys. Med. Biol., Vol. 53, 2008.
[9] P. Bruyndonckx, et al., "Investigation of an in situ position calibration method for continuous crystal-based PET detectors," Nucl. Inst. Meth. A., V. 571(1–2), 2007, 304-307.
[10] A. Gonzalez-Montoro, et al., "Validation of software collimation for the calibration of monolithic PET detector modules," 2018 IEEE Nuclear Science Symposium.
[11] L. A. Pierce, et al., "Multiplexing strategies for monolithic crystal pet detector module," Phys. Med. Biol, vol. 59, 2014.
[12] L. A. Pierce, et al., "Characterization of highly multiplexed monolithic PET / gamma camera detector modules," Phys. Med. Biol, vol. 63, 2018.
[13] A. Gonzalez-Montoro, et al., "Novel Method to Measure the Intrinsic Spatial Resolution in PET Detectors Based on Monolithic Crystals," Nucl. Inst. Phys. Res. A. Vol. 920, pp. 58-67, 11 March 2019.
[14] R. S. Miyaoka, et al., "Resolution properties of a prototype continuous miniature crystal element (cMiCE) scanner," IEEE Trans. Nucl. Sci. 58 2244–9.
[15] A. Gonzalez-Montoro, *et al.*, "Performance study of a large monolithic LYSO PET detector with accurate photon DOI using retroreflective layers," IEEE Trans. Rad. Med. Sc., 2017.
[16] De Berg, et al., Computational Geometry, Springer-Verlag, Berlin, Germany; 1997.
[17] J. B. Davis, et al., "Assessment of 18F PET signals for automatic target volume definition in radiotherapy treatment planning," Radiotherapy Oncol., vol. 80, no. 1, pp. 43–50, 2006.
[18] I. S. Klyuzhin and V. Sossi, "PET image reconstruction and deformable motion correction using unorganized point clouds," IEEE Trans. Med. Imag., vol. 36, no. 6, pp. 1263–1275, Jun. 2017.
[19] H. Alva-Sánchez et al., "Energy calibration of individual crystals in a LYSO pixelated array for microPET detection modules using Voronoi diagrams," Nucl. Instrum. Methods Phys. Res. A Vvol. 596, no. 3, pp. 384–389, 2008.
[20] H. Semmaoui et al., "Crystal identification based on recursive-leastsquares and least-mean-squares autoregressive models for small animal PET," IEEE Trans. Nucl. Sci., vol. 55, no. 5, pp. 2450–2454, Oct. 2008.
[21] G. Van Rossum and F. L. Drake Jr., "Python reference manual". Centrum voor Wiskunde; 1995.
[22] A. Gonzalez-Montoro, et al "Detector block performance based on a monolithic LYSO crystal using a novel signal multiplexing method," Nuc. Inst. Meth. A, 2018.
[23] J. M. Benlloch et al., "Scanner calibration of a small animal PET camera based on continuous LSO crystals and flat panel PSPMTs," Nucl. Instrum. Methods Phys. Res. A Accelerators Spectrometers Detectors Assoc. Equ., vol. 571, nos. 1–2, pp. 26–29, 2007.
[24] S. España, et al., "DigiPET: Sub-millimeter spatial resolution small-animal PETimaging using thin monolithic scintillators," Phys. Med. Biol., vol. 59, no. 13, pp. 3405–3420, 2014.